



## Research Article

# Improving the uniform elongation of ultrafine-grained pure titanium through judicious allocation of work hardening

Jiajun Hu<sup>a</sup>, Dongmei Zhang<sup>a</sup>, Zhaohua Hu<sup>b</sup>, Shuaizhuo Wang<sup>a</sup>, Lirong Xiao<sup>a</sup>, Bo Gao<sup>c</sup>, Dongdi Yin<sup>d</sup>, Hao Zhou<sup>a,\*</sup>, Yonghao Zhao<sup>a,e,\*\*</sup>

<sup>a</sup> Nano and Heterogeneous Materials Center, School of Materials Science and Engineering, Nanjing University of Science and Technology, Nanjing 210094, China

<sup>b</sup> Ansteel Beijing Research Institute Co., Ltd., Beijing 102209, China

<sup>c</sup> Institute of Materials Plainification, Liaoning Academy of Materials, Shenyang 110167, China

<sup>d</sup> Key Laboratory of Advanced Technologies of Materials, Ministry of Education, School of Materials Science and Engineering, Southwest Jiaotong University, Chengdu, Sichuan 610031, China

<sup>e</sup> School of Materials Science and Engineering, Hohai University, Changzhou, 213200, China

## ARTICLE INFO

## Keywords:

Work hardening behavior  
Pure titanium  
Uniform elongation  
<c+a> dislocation

## ABSTRACT

Improving uniform elongation in metals typically involves enhancing the work hardening rate, as elevated work hardening can delay necking and fracture. However, our investigation into commercial pure titanium reveals a counterintuitive relationship between these properties. We find that high uniform elongation correlates with low work hardening capability, while a high work hardening rate results in reduced ductility. Two types of ultrafine-grained pure titanium, prepared by rotary swaging, subsequent rolling, and annealing, exhibit different mechanical properties. Microstructural and deformation mechanism analyses reveal that the difference arise from variations in texture. Specifically, extensive activation of <c+a> dislocations in the former sample leads to premature, intense work hardening that is quickly exhausted, while the latter sample shows a steady, uniform work hardening progression that delays necking. Our findings challenge the conventional understanding that high work hardening rates ensure high uniform elongation. Instead, we propose that optimizing ductility requires a strategic allocation of work hardening throughout the tensile deformation to delay necking. This study reveals the intrinsic relationship between work hardening and ductility, offering new strategies for designing stronger and tougher materials.

## 1. Introduction

With the rapid development of industrial technology, people's demand for material strength is increasing day by day [1]. The application of high-strength materials is beneficial for lightweight design of structural components, especially for fields such as transportation and aerospace, which is an effective way to reduce fuel consumption and greenhouse gas emissions [2,3]. However, there is often a trade-off between strength and ductility (uniform elongation), and good ductility is the guarantee of material formability (low ductility leads to strain localization during the machining process, inducing the generation of cracks) [4]. Based on this, a series of processes have been developed to improve material ductility and thus enhance formability, for example,

hot forming [5], current or ultrasonic assisted forming [6,7]. But these methods require specific deformation conditions and also impact the strength of the material. Therefore, while maintaining strength, maximizing the ductility of materials has remain a long-standing challenge for material researchers.

Usually, the localized deformation (i.e. necking instability) of materials during tensile tests can be predicted through the Considere criterion [8]:

$$\left(\frac{\partial\sigma}{\partial\varepsilon}\right)_\varepsilon \leq \sigma \quad (1)$$

where  $\sigma$  and  $\varepsilon$  are true stress and true strain, respectively, and  $\dot{\varepsilon}$  denote strain rate.  $\partial\sigma/\partial\varepsilon$  is work hardening rate  $\Theta$ . It is generally believed that a

\* Corresponding author.

\*\* Corresponding author at: Nano and Heterogeneous Materials Center, School of Materials Science and Engineering, Nanjing University of Science and Technology, Nanjing 210094, China.

E-mail addresses: [hzhou511@njust.edu.cn](mailto:hzhou511@njust.edu.cn) (H. Zhou), [yhzha@njust.edu.cn](mailto:yhzha@njust.edu.cn) (Y. Zhao).

<https://doi.org/10.1016/j.jmatprotec.2024.118484>

Received 18 April 2024; Received in revised form 14 June 2024; Accepted 14 June 2024

Available online 16 June 2024

0924-0136/© 2024 Published by Elsevier B.V.

higher work hardening can delay the occurrence of necking, produces larger uniform elongation [9]. Such as, during the tensile deformation process of coarse grained pure titanium (Ti) in liquid nitrogen environment, the rich twinning mechanisms greatly enhance its work hardening ability, resulting in a significant improvement in its uniform elongation compared to room temperature stretching [10]. Nanocrystalline (NC) metal have extremely high strength, but due to their extremely small grain size, grain boundaries are more likely to absorb dislocations, making it difficult to accumulate dislocations within grains, resulting in low work hardening ability and subsequently low ductility [11]. Therefore, the guiding ideology of many currently developed strengthening and toughening schemes is mainly to increase the accumulation dislocations to improve work hardening ability and ductility [12,13].

However, the above criteria are only a rough understanding, and in fact, ductility is a process variable, which closely related to the work hardening ability at each moment during the tension process. As schematically shown in Fig. 1, excessive work hardening ability can cause the true stress-strain curve to rise too quickly and intersect with the work hardening rate curve prematurely (the red tensile curve of pure magnesium [14], also observed in pure Ti [15]), although low work hardening ability also leads to the early generation of necking due to the quick drop of the work hardening rate curve (the blue tensile curve of nano or ultrafine grained (UFG) metals [16]). In tensile tests, the descending work hardening rate curve and the ascending true stress-strain curve usually run in opposite directions, destined to inevitably intersect. Therefore, the key to improving ductility lies in how to delay the meeting of the work hardening rate curve and the true stress-strain curve as much as possible, as shown by the dotted black curves in Fig. 1.

Titanium, with its characteristic hexagonal close-packed (HCP) crystal structure, typically exhibits significant elastic-plastic anisotropy [17]. The strength of coarse-grained pure Ti is relatively low, so its application is limited, the typical strengthening strategy is to refine grains through severe plastic deformation (SPD), which include high-pressure torsion [18,19], equal channel angular pressing [20], rotary swaging [21,22], and accumulative roll bonding, et al. [23]. During the process of SPD, twinning and dislocations continuously refine the grains, thereby obtaining ultrafine or nano grain structures. But due to the almost saturated defect density, the UFG pure Ti obtained through SPD often loses the defects accumulate ability, leading to early necking [8]. This can be improved by appropriate annealing parameters.

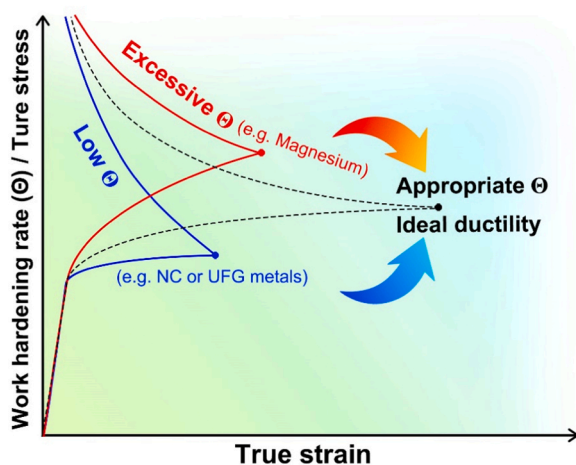


Fig. 1. Schematic representation of the relationship between uniform elongation (necking onset) and work hardening rate  $\Theta$ . Both too high (red curve) and too low (blue curve)  $\Theta$  cause too early necking onset, while reasonable  $\Theta$  distribution (dotted black curve) during the stretching process can delay necking onset and increase uniform elongation.

For UFG pure Ti, twinning is notably limited due to grain size effects [24], resulting in deformation predominantly governed by dislocation slipping. On the other hand, the reduction of grain size increases the yield strength of pure Ti, which can promote the activation of  $\langle c+a \rangle$  type pyramidal slip [25], which becomes the critical mechanism to accommodate c-axis deformation, enhancing work hardening capability [26]. This has led researchers to focus on promoting  $\langle c+a \rangle$  pyramidal slip in HCP metals to improve both work hardening ability and ductility [27]. However, it remains uncertain whether an elevated work hardening capability necessarily translates to improved ductility at comparable yield strength levels.

In this work, we selected HCP commercial pure Ti as the model material to investigate the relationship between work hardening ability and ductility, given its strong correlation with texture type [28]. We prepared two UFG pure Ti samples with different texture types but similar grain sizes through thermomechanical treatment. The heat treatment during preparation released internal stresses, ensuring the UFG structure remained stable during loading. We found that the activation of  $\langle c+a \rangle$  dislocations significantly increased the work hardening exponent of the HCP pure Ti but did not result in the anticipated high ductility, contrary to traditional expectations. It is well known that the work hardening ability is closely related to dislocation behavior [29]. To understand the underlying mechanism of this unexpected result, we investigated the dislocation activities in the two samples using transmission electron microscopy (TEM) and visco-plastic self-consistent (VPSC) simulations. Our findings indicate that high work hardening in the early stages of deformation depletes the dislocation storage capacity for later stages, leading to premature necking. Thus, we propose a new perspective: achieving improved uniform elongation and ductility requires a balanced distribution of the work hardening rate ( $\Theta$ ) throughout the deformation process.

## 2. Material and methods

### 2.1. Experimental material

Polycrystalline commercially pure titanium (CP-Ti) rod with ASTM Grade 1 was used in this study. The detailed chemical composition (wt %) of the material was as follows: 0.009% C, 0.005% H, 0.1% O, 0.012% N, 0.021% Fe, and balance Ti. The average grain size of the CP-Ti was  $\sim 15 \mu\text{m}$ .

### 2.2. Preparation of the samples

A four-die rotary swaging machine was employed to process the CP-Ti rod. The principle of rotary swaging is shown in Fig. 2a. During the swaging process, four dies were evenly arranged around the circumference of the CP-Ti rod, rotating at high speed around the rod while simultaneously making high-frequency short-range strokes along the radial direction. The initial rod, with a diameter of 35 mm, was reduced to a final diameter of 7.8 mm, achieving an equivalent strain ( $\epsilon$ ) of 3.0. The equivalent strain was calculated using the following equation:

$$\epsilon = \ln(A_0/A) \quad (1)$$

where  $A_0$  and  $A$  are the initial and final cross-sectional areas of the rod, respectively. The swaged sample was referred to as the rotary swaging (RS) sample. Subsequently, the RS sample was subjected to rolling using a rolling machine with a roller diameter of 120 mm and a rolling speed of 0.34 m/s. The RS sample was rolled to a final thickness of 1 mm after  $\sim 30$  rolling passes, achieving a total rolling reduction of 87%. This rolled sample was referred to as the rotary swaging-rolling (RSR) sample, and its process diagram is shown in Fig. 2b. After deformation processing, both the RS and RSR samples were annealed at  $450^\circ\text{C}$  for 30 minutes. The annealed samples were referred to as RS-A and RSR-A samples, respectively.

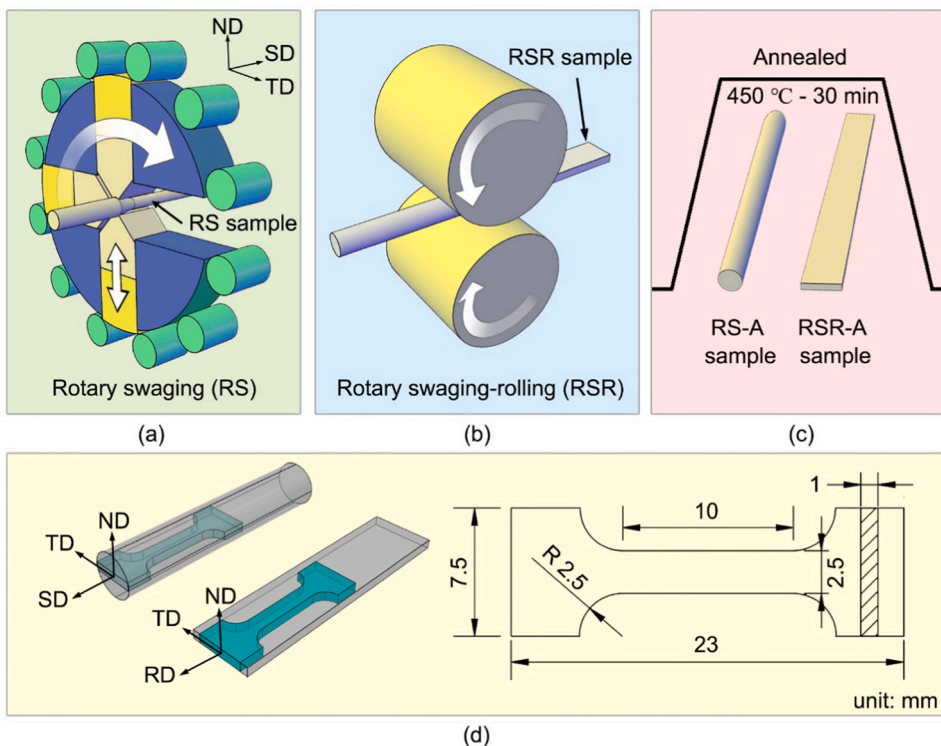


Fig. 2. Process schematic diagram: (a) rotary swaging (RS); (b) rotary swaging-rolling (RSR); (c) heat treatment; (d) Geometric dimension and cut position of tensile specimen. The sample coordinates were defined by the swaging direction (SD), rolling direction (RD), normal direction (ND) and transverse direction (TD).

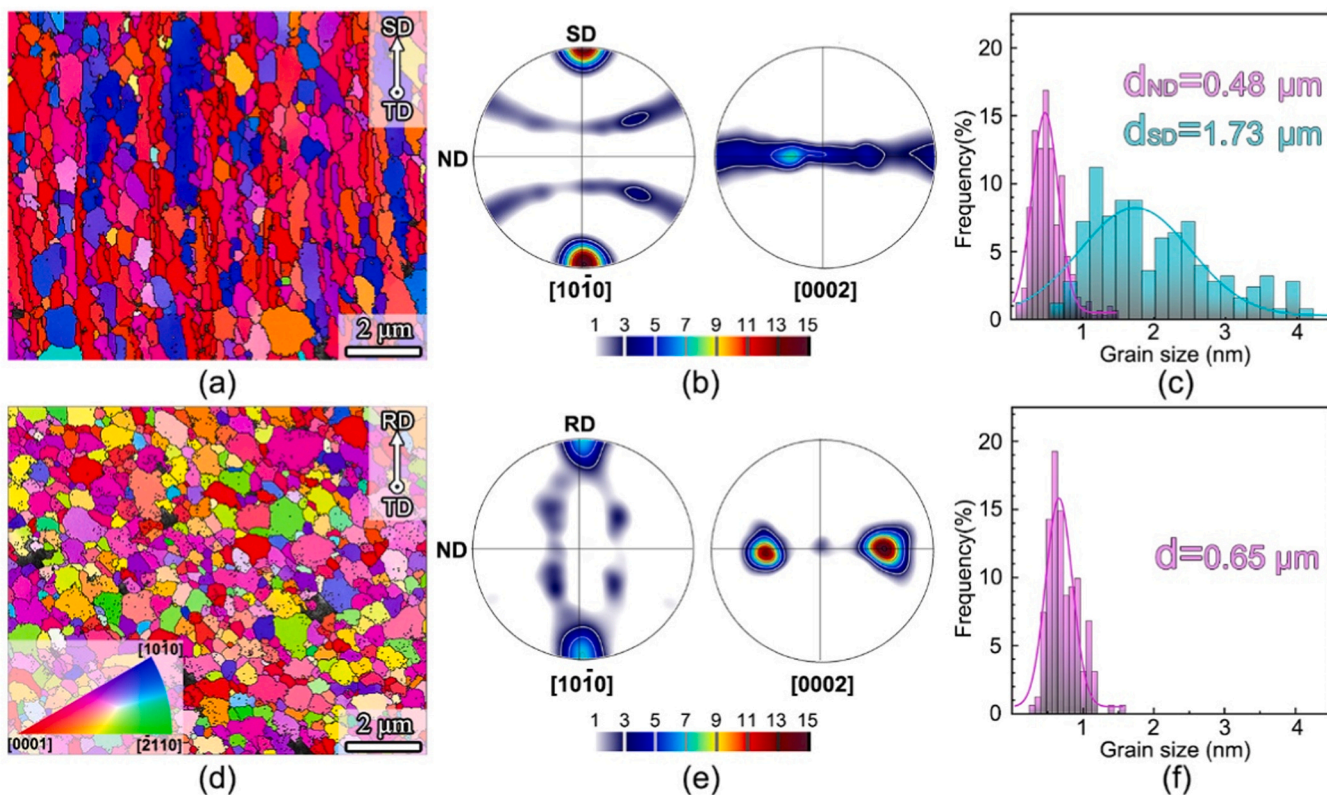


Fig. 3. The microstructure of rotary swaged sample after annealed (RS-A) and rotary swaging-rolled sample after annealed (RSR-A): (a-c) IPF map, pole figures and grain size distribution statistics of RS-A sample, respectively; (d-f) IPF map, pole figures and grain size distribution statistics of RSR-A sample, respectively.

### 2.3. Mechanical testing and microstructure characterization

Tensile specimens were prepared by cutting them from the center of swaged and rolled samples using wire cutting. The geometric dimensions of the tensile samples were shown in Fig. 2d. Uniaxial tensile tests were performed using a Walter + Baiag LFM 20 kN tensile testing machine equipped with an extensometer, applying a strain rate of  $1 \times 10^{-3} \text{ s}^{-1}$ . To ensure accuracy and reliability, all tensile specimens underwent a gradual polishing process, ranging from 400# to 2000# sandpapers. Each tensile test was repeated at least three times for statistical validity.

Microstructural characterization was carried out using advanced microscopy techniques. A transmission electron microscope (TEM TECNAI 20) and a high-resolution field emission Carl Zeiss Auriga scanning electron microscope (SEM) were employed for this purpose. The SEM was equipped with an Oxford Instruments Aztec 2.0 EBSD system (Channel 5 software) for electron backscatter diffraction (EBSD) mapping. Metallographic samples were obtained from the center of swaged rods for microscopy analysis. For EBSD characterization, specimens were mechanically polished with SiC paper and then electropolished in a solution containing 90 vol% acetic acid and 10 vol% perchloric acid using a Buehler Electro Met 4 polisher. The electropolishing process involved applying a voltage of 35 V for 60 s. For TEM characterization, samples were polished to a thickness of 60  $\mu\text{m}$  using sandpaper and then punched into discs with a diameter of 3 mm. Perforation was achieved by twin-jet electropolishing using a solution comprising 10 vol% perchloric acid and 90 vol% ethyl alcohol.

## 3. Results

### 3.1. Microstructure

The microstructures of the RS-A and RSR-A samples were analyzed using inverse pole figure (IPF) maps along the transverse direction (TD), as shown in Fig. 3a and d. The RS-A sample exhibits a microstructure predominantly composed of fibrous grains along with some equiaxed recrystallized grains, whereas the RSR-A sample is mainly composed of

equiaxed grains. Notably, these samples display significantly different texture types. For the RS-A sample, a strong  $\langle 10\bar{1}0 \rangle$  fibrous texture is observed along the swaging direction (SD), with the  $\langle 0002 \rangle$  texture parallel to the normal direction (ND). This texture is characteristic of rotary swaged titanium (Ti) [30], and is illustrated in Fig. 3b. Conversely, the RSR-A sample exhibits a shift in the maximum pole intensity from the  $\{10\bar{1}0\}$  plane to the  $\{0002\}$  plane, resulting in a bimodal basal texture similar to that of rolled CP-Ti [31], and shown in Fig. 3e. The average grain sizes for both RS-A and RSR-A samples were measured using the line-intercept method. For the RS-A sample, the grain size distribution along the ND and the SD is plotted in Fig. 3c, represented by  $d_{\text{ND}}$  and  $d_{\text{SD}}$ . The average width and length of the fibrous grains in the RS-A sample are approximately 0.48  $\mu\text{m}$  and 1.73  $\mu\text{m}$ , respectively. In contrast, the equiaxed grains of the RSR-A sample have an average diameter of approximately 0.65  $\mu\text{m}$ , as shown in Fig. 3f. These grain sizes are similar and are classified as ultrafine grains, being less than 1  $\mu\text{m}$  [23]. This analysis highlights the distinct microstructural and textural differences between the RS-A and RSR-A samples, contributing to their unique mechanical properties and behavior under various processing conditions.

Fig. 4 illustrates the microstructural evolutions of CP-Ti samples following distinct deformation processes and subsequent annealing, as revealed by TEM. Fig. 4a shows the transverse direction TEM image of the RS sample, exhibiting a refined, elongated grain structure oriented along the swaging direction, resulting in a fibrous-grained microstructure with an average width of  $\sim 140 \text{ nm}$ . In contrast, Fig. 4b shows the microstructure post rolling deformation, where the fibrous grains have been fragmented into equiaxed grains with an estimated diameter of  $\sim 126 \text{ nm}$ , closely matching the fibrous grain width observed in the RS sample. Fig. 4c shows the microstructure of the RS-A sample after annealing, which comprises a mixture of fibrous grains and partially recrystallized equiaxed grains. Notably, the grain shape largely retains the characteristics of the pre-annealing state. Fig. 4d shows the RSR-A sample's microstructure post combined swaging-rolling deformation and annealing, characterized by a predominantly equiaxed grain structure. The grain shapes in the RSR-A sample also maintain the pre-annealing characteristics.

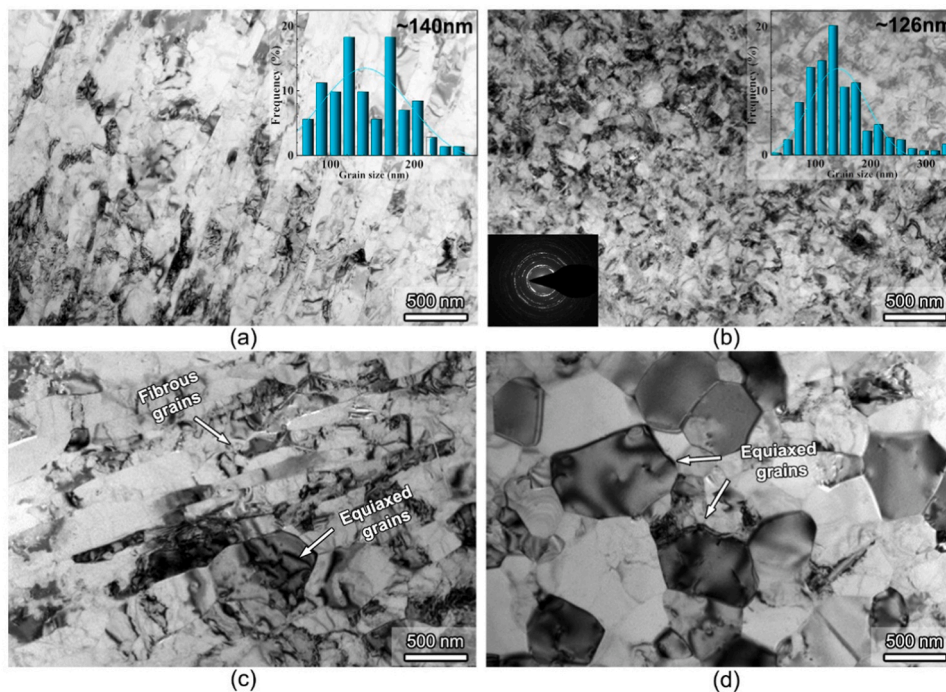


**Fig. 4.** TEM bright field micrographs of CP-Ti observed from the transverse direction (TD): (a) rotary swaging (RS); (b) rotary swaging-rolling (RSR); (c) rotary swaged sample after annealed (RS-A); (d) rotary swaging-rolled sample after annealed (RSR-A).

3.2. Mechanical property

Fig. 5a shows the engineering stress-strain curves for the RS and RSR samples, along with their subsequent annealed counterparts. Post-deformation, the ultimate tensile strength (UTS) of the RS and RSR samples exhibits a significant increase from 318 MPa to 817 MPa and 887 MPa, respectively, while the total elongation (TE) decreases from 50.7% to 9.6% and 6.7%. Upon annealing, the UTS of the RS-A and RSR-A samples decreases to 636 MPa and 592 MPa, respectively, with a concomitant recovery in uniform elongation (UE) and TE to 9.5% and 11.7%, and 21.7% and 23.6%, respectively. Detailed mechanical properties are shown in Fig. 5b. Notably, although the yield strength (YS) of the RS-A sample (498 MPa) is slightly lower than that of the RSR-A sample (540 MPa), the RS-A sample exhibits a higher UTS, indicating superior work hardening capacity compared to the RSR-A sample. The work hardening behavior of the RS-A and RSR-A samples diverges significantly, as illustrated in Fig. 5c, which plots the work hardening

rate against true strain. Initially, the RS-A sample exhibits a markedly higher work hardening rate than the RSR-A sample; however, this rate diminishes rapidly with increasing true strain. In contrast, the RSR-A sample maintains a linear and uniform work hardening rate throughout the deformation process. Fig. 5d further indicates this difference by showing the increment of flow stress ( $\Delta\sigma$ , i.e.  $\sigma_f - \sigma_{0.2}$ ) versus true strain; the  $\Delta\sigma$  of the RS-A sample surpasses that of the RSR-A sample, clearly demonstrating the RS-A sample's enhanced work hardening ability. This trend is consistently observed under other annealing parameters, as corroborated by tensile test results in Fig. 5e-f.

The work hardening behavior of metallic materials can be described using Taylor's equation [32]:

$$\Delta\sigma = M_T \alpha G b \sqrt{\Delta\rho} \tag{2}$$

where  $M_T$  represents the Taylor factor,  $\alpha$ ,  $G$  and  $b$  are a geometrical coefficient, the shear modulus, and the Burgers vector, respectively.

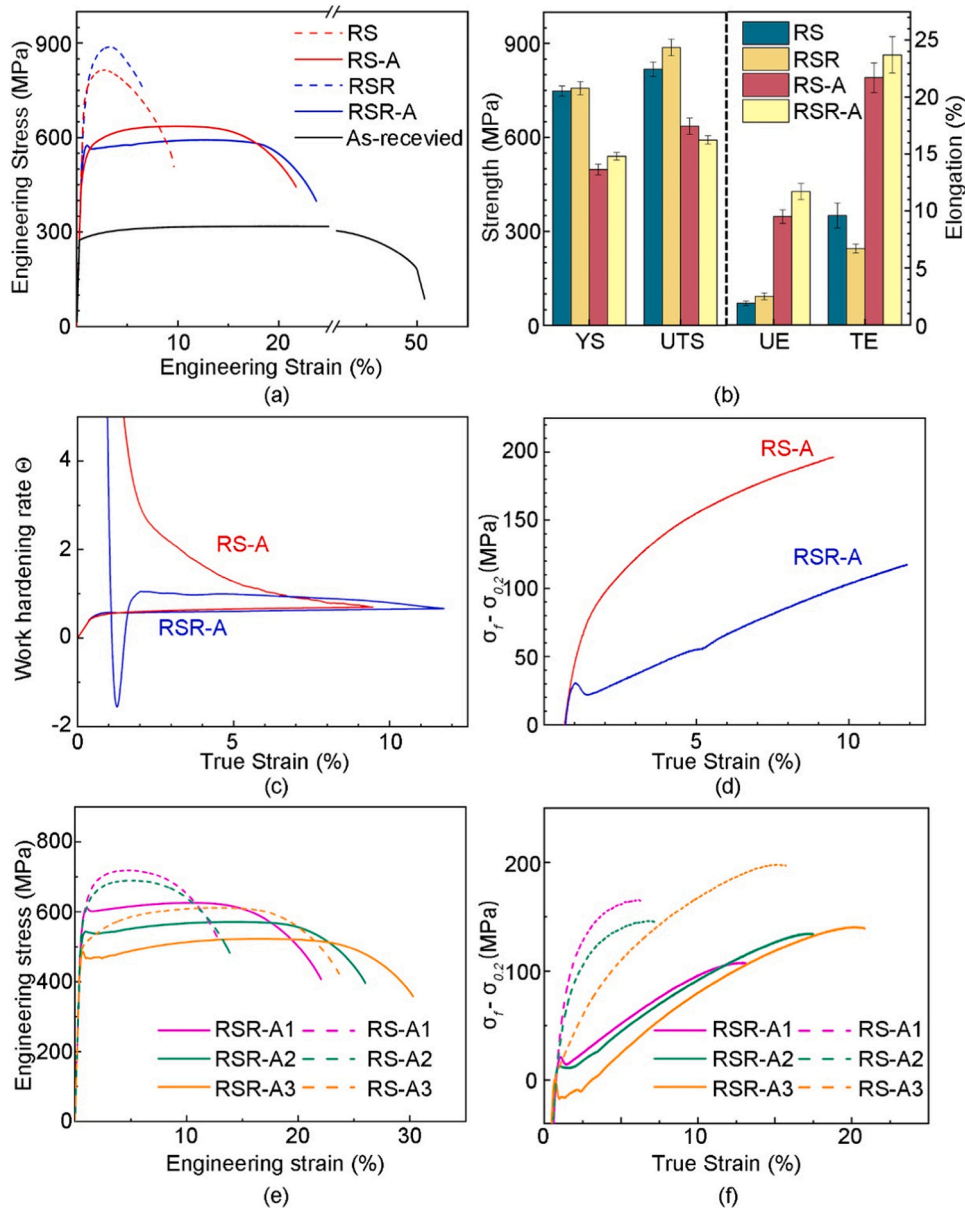


Fig. 5. Mechanical properties of CP-Ti under different treatments: (a) Engineering stress-strain curves; (b) specific mechanical property parameters, error bars represent  $\pm$  standard deviation (SD) from the mean value ( $n = 3$ ); (c) true stress and work hardening curves from tensile tests; (d) flow true stress (minus YS) versus true strain curves; (e-f) engineering stress-strain curves and flow true stress versus true strain curves under the other annealing parameters, where A1 (450°C/10 min), A2 (500°C/2 min) and A3 (500°C/5 min).

From the equation, the increment in flow stress  $\Delta\sigma$  is proportional to the square root of the increment in dislocation density  $\Delta\rho$ . It can be inferred that the dislocation proliferation rate of the RS-A sample is higher than that of the RSR-A sample during the initial stages of deformation. However, due to a rapid decrease, the RS-A sample's dislocation proliferation rate becomes lower than that of the RSR-A sample in the later stages of deformation. This suggests that the high work hardening capacity of the RS-A sample in the early stage depletes its dislocation storage capacity more quickly, leading to an earlier onset of necking.

In addition to work hardening rate, another parameter for evaluating strain hardening capability is work hardening exponent  $n$ , as determined by the Ludwick equation [33]:

$$\sigma = \sigma_0 + K\varepsilon_p^n \quad (3)$$

where  $n$  is the work hardening exponent,  $K$  is the strength coefficient,  $\sigma$  is the true stress,  $\sigma_0$  is the yield strength and  $\varepsilon_p$  is the true plastic strain. The  $n$  value indicates the ability of the material to undergo uniform deformation through hardening before necking occurs [34]. A high  $n$  value means better work hardening ability and uniform deformation. The simulated  $n$  value, shown in Fig. 6, are 0.32 for RS-A, and 0.21 for RSR-A, indicating that RS-A samples have a higher work hardening capability. However, further analysis of the  $n$  value across different stages of uniform plastic deformation reveals an interesting phenomenon: as the strain increases, the  $n$  value for RS-A continuously decreases from 0.36 to 0.21, while for RSR-A, it increases from 0.13 to 0.32. This indicates that although the RS-A sample exhibits high work hardening ability in the early stage of deformation, this ability rapidly diminishes with increasing strain, reducing the uniform plastic deformation capacity and leading to necking. Consequently, the RS-A sample ultimately shows a lower uniform elongation rate compared to the RSR-A sample, which has a poorer initial work hardening ability.

### 3.3. Dislocation configurations after deformation

In general, the two primary mechanisms responsible for the plasticity of materials are dislocation slip and deformation twinning. Noted that, the deformation twinning of Ti is strongly affected by the grain size; when the grain size is less than  $1\mu\text{m}$ , deformation twins are completely replaced by dislocation slip [24]. In this work, the microstructure of RS-A and RSR-A samples consists of ultrafine grain, with size less than  $1\mu\text{m}$ . Consequently, their twinning behavior during deformation is significantly inhibited. Therefore, it is hypothesized that the variation in dislocation slip mode is the source of the difference in work hardening behavior between the RS-A and RSR-A samples. To identify the active slip systems in deformed RS-A and RSR-A samples, two-beam conditions were set during TEM observations according to the invisibility criterion of  $g \cdot b = 0$ , where  $g$  and  $b$  represent the reflection vector and Burgers vector, respectively. When a particular reflection is set as  $g = 0\bar{1}10$  or  $g = 2\bar{1}\bar{1}0$ ,  $\langle a \rangle$  dislocations with  $b = \frac{1}{3} \langle 11\bar{2}0 \rangle$  become visible, and  $\langle c \rangle$  dislocations with  $b = \langle 0001 \rangle$  are invisible in bright field TEM images. Conversely, when the two-beam situations are set as  $g = 0002$ ,  $\langle a \rangle$  dislocations become invisible while  $\langle c \rangle$  dislocations are visible. In addition,  $\langle c+a \rangle$  dislocations with  $b = \frac{1}{3} \langle 11\bar{2}3 \rangle$  are visible in all aforementioned two-beam conditions. Therefore, the dislocation type can be determined by two-beam bright-field (TBDF) technology [35].

Figs. 7a-1 and b-1 show the dislocation configurations in the RS-A and RSR-A samples deformed to 10% strain, respectively. As expected, deformation twinning is inhibited in UFG pure Ti, and the primary deformation mechanism is dislocation slip. Detailed two-beam bright-field TEM imaging was carried out for the RS-A sample near  $[2\bar{1}\bar{1}0]$  zone axis under  $g = 0\bar{1}10$  (Figs. 7a-2) and  $g = 0002$  (Figs. 7a-3). In the  $g = 0\bar{1}10$  condition, all dislocations are visible, whereas in the  $g = 0002$  condition, some dislocations become invisible while others remain, indicating the presence of both  $\langle a \rangle$  and  $\langle c+a \rangle$  type dislocations,

marked by red and blue arrows, respectively, in Figs. 7a-3. In contrast, the dislocation types activated during the deformation of RSR-A sample differ significantly from those of the RS-A sample. TEM imaging under  $g = 0\bar{1}10$  (Figs. 7b-2), and  $g = 0002$  (Figs. 7b-3) shows that most dislocations are eliminated under the  $g = 0002$  condition, with only a small portion remaining visible. This indicates that primarily  $\langle a \rangle$  dislocations form in the deformed RSR-A sample, with the activation of  $\langle c+a \rangle$  dislocations being more challenging. According to the TBDF method, the activation of  $\langle c+a \rangle$  type dislocations is likely responsible for the distinct work hardening behaviors observed in the RS-A and RSR-A samples.

### 3.4. Visco-plastic self-consistent (VPSC) modeling

Although the activation of different dislocation types during deformation of RS-A and RSR-A samples was observed by TBDF method, the limited observation area in TEM restricts the ability to obtain comprehensive statistical results. To address this limitation, the visco-plastic self-consistent (VPSC) model can be employed to simulate the plastic deformation behavior of polycrystals [36]. This model predicts the relative activity of slip and twin systems, providing results based on the macro polycrystalline scale. Consequently, the VPSC model can complement the TBDF method, offering a broader and more statistically understanding of the deformation mechanisms.

The VPSC model, initially developed by Molinari et al. and extended for fully anisotropic behavior by Lebensohn and Tomé [37], is capable of predicting the anisotropic plastic deformation of a polycrystal. Renowned for its high forecasting accuracy, exceptional computational efficiency and robust algorithms, the VPSC model has gained wide acceptance [38]. In recent years, it has been effectively employed to replicate the texture formation [39] and predict the activity of twinning and slip system during plastic deformation [40]. In the present investigation, the VPSC model is used to simulate the plastic deformation behavior of RS-A and RSR-A samples. The VPSC-7d software package was utilized to predict the experimental stress-strain curve and local texture evolution under the stress triaxiality conditions. The self-consistent model considers each grain as an ellipsoidal viscoplastic inclusion surrounded by a homogeneous medium representing the average response of the surrounding grains. In the simulations, the value of threshold stress ( $\tau^s$ ) was updated during plastic deformation by the Voce hardening model. This model characterizes the evolution of threshold stress with accumulated shear strain in each grain using the following from:

$$\tau^s = \tau_0^s + (\tau_1^s + \theta_1^s \Gamma) (1 - \exp(-\Gamma \frac{\theta_0^s}{\tau_1^s})) \quad (4)$$

where  $\Gamma = \sum_s \Delta\gamma^s$  is the accumulated shear in the grain,  $\tau_0$ ,  $\theta_0$ ,  $\theta_1$ ,  $(\tau_0 + \tau_1)$  are the initial CRSS, the initial hardening rate, the asymptotic hardening rate and the back-extrapolated CRSS, respective.

In this work, the self-consistent schemes were used with the  $n^{\text{eff}} = 10$ , The initial ellipsoid ratios of RSeD sample set as 1:3:1, reflecting the long and short axis ratios determined from EBSD statistical results. Conversely, the grains of RSRed samples are equiaxed, and their initial ellipsoid ratios were set as 1:1:1. The material parameters determined for the  $n^{\text{eff}} = 10$  self-consistent schemes are summarized in Table 1. The elasticity constants of Ti are listed in Table 2.

In this study, deformation twinning is significantly inhibited in the RS-A and RSR-A samples due to grain size effect. Consequently, the VPSC model considers only dislocation slip activities, specifically the basal  $\langle a \rangle$  ( $\{0002\}\langle 11\bar{2}0 \rangle$ ) slip, the prismatic  $\langle a \rangle$  ( $\{1\bar{1}00\}\langle 11\bar{2}0 \rangle$ ) slip, and the pyramidal  $\langle c+a \rangle$  ( $\{1\bar{1}01\}\langle 11\bar{2}3 \rangle$ ) slip, while ignoring the influence of twins. The true stress-true strain curves simulated by the VPSC model are shown in Fig. 8. After numerous trials to calibrate the simulate parameters, a good consistency between the simulated and

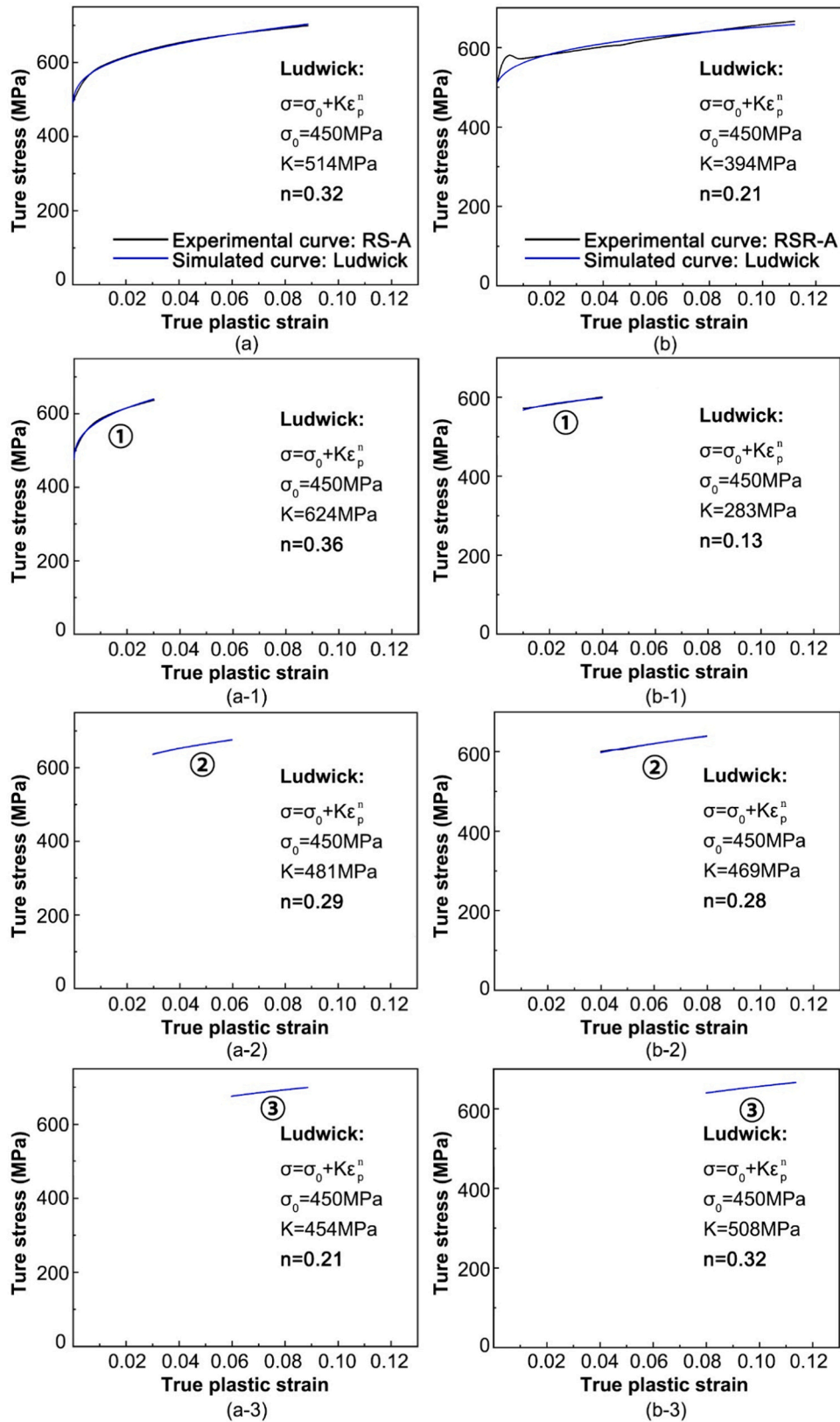


**Fig. 6.** Experimental true stress versus true plastic strain curves and Ludwick simulated curves of the rotary swaged sample after annealed (RS-A) and rotary swaging-rolled sample after annealed (RSR-A): (a) RS-A sample, (a-1), (a-2) and (a-3) are the simulated results at different stages of uniform plastic deformation, respectively; (b) RSR-A sample, (b-1), (b-2) and (b-3) are the simulated results at different stages of uniform plastic deformation, respectively.

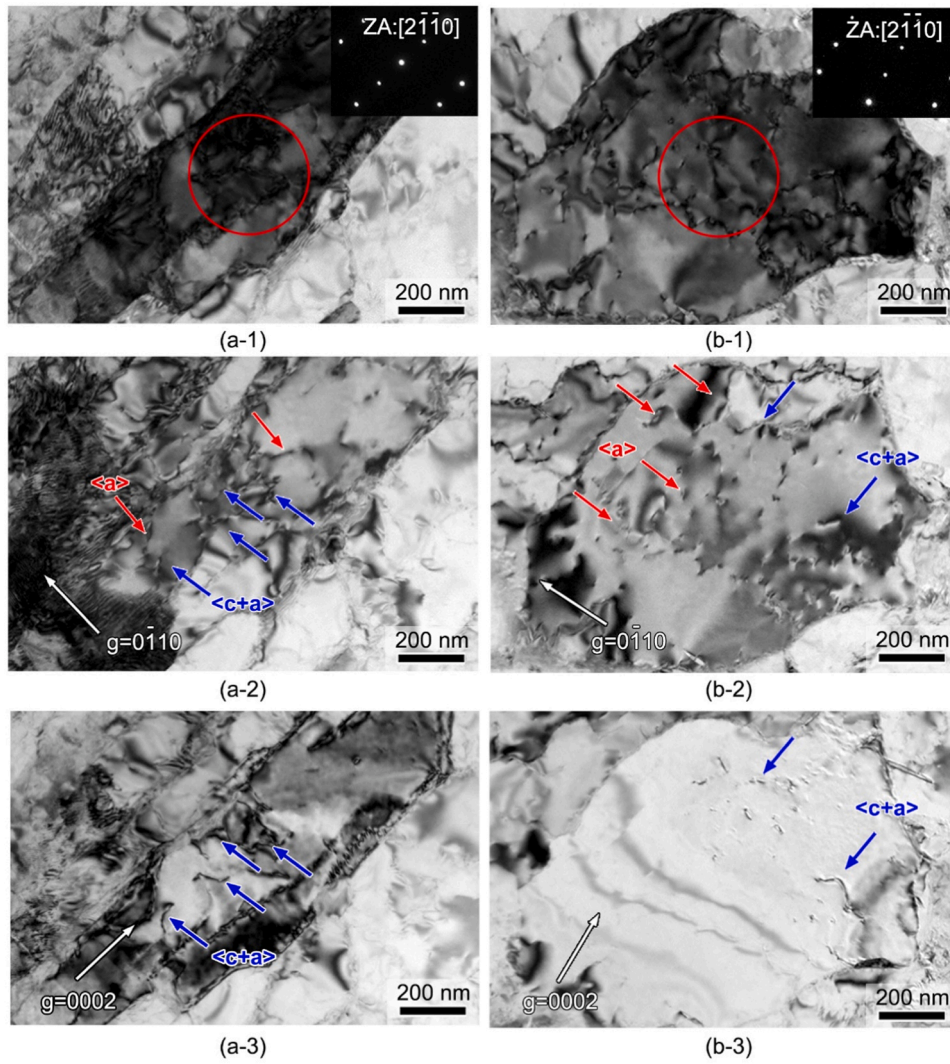


Fig. 7. Dislocation configurations in the rotary swaged sample after annealed (RS-A) and rotary swaging-rolled sample after annealed (RSR-A) under tensile-deformed to 10%: (a-1) RS-A sample under deformation at  $[2\bar{1}\bar{1}0]$  zone axis, (a-2)  $g = 0\bar{1}10$  in TBDF, (a-3)  $g = 0002$  in TBDF; (b-1) RS-A sample under deformation at  $[2\bar{1}\bar{1}0]$  zone axis, (b-2)  $g = 0\bar{1}10$  in TBDF, (b-3)  $g = 0002$  in TBDF.

Table 1  
Material Voce hardening parameters with  $n^{eff} = 10$  self-consistent schemes.

	Mode	$\tau_0$	$\tau_1$	$\theta_0$	$\theta_1$
RSed	Basal	300	30	400	10
	Prismatic	125	30	600	40
	Pyramidal	425	60	400	10
RSRed	Basal	160	20	1000	20
	Prismatic	50	20	1000	160
	Pyramidal	175	35	1000	10

Table 2  
The elasticity constants of pure titanium [36].

Elasticity constants (GPa)				
C11	C12	C13	C33	C44
160	90	66	181	46.5

experimental stress-strain curves was achieved (the VPSC model only simulates plastic deformation stage). Fig. 8 also compares the simulated deformation texture with the experimental measurements, where the pole figures are generated using MTEX toolbox in Matlab software. The

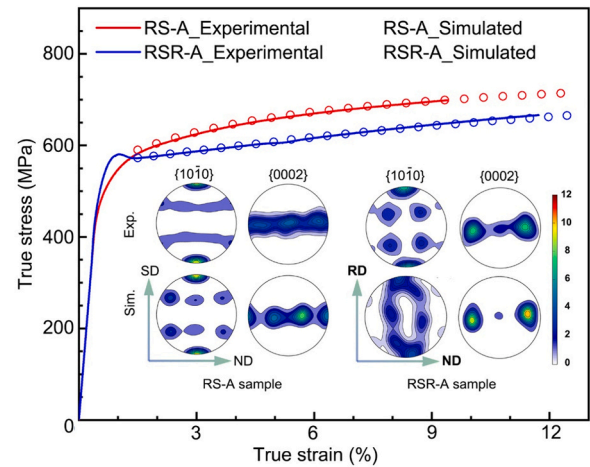


Fig. 8. Comparison between experimental and simulated true stress-strain curves and texture of the rotary swaged sample after annealed (RS-A) and rotary swaging-rolled sample after annealed (RSR-A).

simulated pole figures show a good agreement with the experimental results.

The simulated relative slip system activities as a function of plastic strains are shown in Fig. 9. The VPSC simulation results show significant differences in the activation of slip systems during tensile deformation in RS-A and RSR-A samples. For the RS-A sample, the prismatic  $\langle a \rangle$  slip system exhibits higher activation than the other two modes at the initial stage of deformation. As the strain increases, the activation of prismatic  $\langle a \rangle$  and basal  $\langle a \rangle$  slip systems decreases, while the pyramidal  $\langle c+a \rangle$  slip system gradually becomes dominant. In contrast, for the RSR-A sample, the simulation results reveal that tensile deformation is primarily dominated by the prismatic  $\langle a \rangle$  slip system, with partial activation of the pyramidal  $\langle c+a \rangle$  slip system, while the basal  $\langle a \rangle$  slip system is difficult to activate. The relative slip systems activities align with the observations from the TBDF analysis (Fig. 7). Overall, these results indicate that RS-A sample can activate various slip modes during deformation, while the RSR-A sample predominantly utilizes the prismatic  $\langle a \rangle$  slip with a minor contribution from  $\langle c+a \rangle$  slip.

#### 4. Discussion

The activation of slip system is closely related to the Schmid factor (SF), which serves as a predictor for the likelihood of slip system activation under specific loading directions [41]. The SF is often employed to estimate the ease of slip operation, influenced significantly by the texture of the material. In this study, RS-A and RSR-A samples show different texture types (as shown in Fig. 3b and e), which impact their SF distributions. Fig. 10 shows the Schmid factor distributions of the three slip systems in the RS-A and RSR-A samples, with the loading direction along SD and RD, respectively. For the RS-A sample, the distribution indicates that the pyramidal  $\langle c+a \rangle$  slip, with an average Schmid factor of 0.401, is most likely to be activated. In addition, the basal  $\langle a \rangle$  slip, with an average SF of 0.335, is also a relatively soft slip mode. However, the prismatic  $\langle a \rangle$  slip, with an average SF of 0.268, represents a harder slip mode. In contrast, the RSR-A sample shows different tendencies. The prismatic  $\langle a \rangle$  and pyramidal  $\langle c+a \rangle$  slip systems, with average Schmid factors of 0.449 and 0.451, respectively, are more likely to be activated. Conversely, the basal  $\langle a \rangle$  slip, with an average Schmid factor of 0.154 is less likely to be initiated.

In addition to high Schmid factor, low critical resolved shear stress (CRSS) is important for promoting the activation of various slip systems [25]. The Schmid factor denotes the resolved shear stress (RSS) of the applied stress ( $\sigma_{\text{applied}}$ ) on specific slip planes. Therefore, knowing the SF

and CRSS allows for the calculation of the  $\sigma_{\text{applied}}$  needed to stimulate dislocation movement using the following equation::

$$\sigma_{\text{applied}} = \sigma_{\text{CRSS}}/m \quad (5)$$

where  $m$  is the Schmid factor of corresponding slip system [42]. For pure Ti with a  $c/a$  ratio of 1.587, prismatic glide is generally easier to activate than basal glide due to this ratio being less than the ideal 1.633 [43]. Based on previous studies [44], the CRSS values to activate basal, pyramidal and prismatic slip systems are 150 MPa, 120 MPa, and 30 MPa, respectively. The calculated  $\sigma_{\text{applied}}$  for activating different slip systems in RS-A and RSR-A samples is shown in Table 3. For the RS-A sample, the stress required to activate all three slip modes is less than the flow stress observed in tensile tests, suggesting that these slip modes can be started. The Schmid factor of the pyramidal  $\langle c+a \rangle$  slip is the highest among these slip modes. In contrast, for the RSR-A sample, the Schmid factors for pyramidal  $\langle c+a \rangle$  slip and prismatic  $\langle a \rangle$  slip are nearly equivalent. However, the CRSS for prismatic  $\langle a \rangle$  slip is significantly lower than that for pyramidal  $\langle c+a \rangle$  slip, indicating that the prismatic  $\langle a \rangle$  slip is largely activated during deformation. In addition, the basal  $\langle a \rangle$  slip is difficult to activate due to its low Schmid factor and high CRSS, as indicated by the calculations in Table 3. These findings align with the simulation results shown in Fig. 9.

The observed differences in work hardening behaviors between the RS-A and RSR-A samples are related to the activation of distinct slip systems. Work hardening results from the interactions of dislocations gliding on intersecting slip planes. These interactions lead to dislocation entanglement, which inhibits dislocation motion and produces a strengthening effect [45]. In this research, the RS-A sample activates the basal  $\langle a \rangle$  slip system during deformation, while the RSR-A sample finds it difficult to activate this mode. The activation of more slip systems in the RS-A sample facilitates greater dislocation interactions, resulting in a faster increase in dislocation density. On the other hand, both VPSC simulation and TEM observations show that a large number of  $\langle c+a \rangle$  dislocations are activated in the RS-A sample, while  $\langle c+a \rangle$  dislocations are relatively inactive in RSR-A samples. Yu et al. reported the detailed source mechanism of  $\langle c+a \rangle$  dislocation slip in Ti alloys [26], demonstrating through in situ nano compression and TEM that  $\langle c+a \rangle$  dislocation initiation follows  $\langle a \rangle$  dislocation activity. They found that  $\langle c+a \rangle$  dislocation junctions form when  $\langle a \rangle$  segments on the prism plane encounter pre-existing  $\langle c \rangle$  segments, subsequently allowing  $\langle c+a \rangle$  dislocations to cross slips from the prism plane (immobile) to the pyramidal plane (mobile). This nucleation and emission of  $\langle c+a \rangle$  dislocations contribute to pronounced work hardening, attributed to the

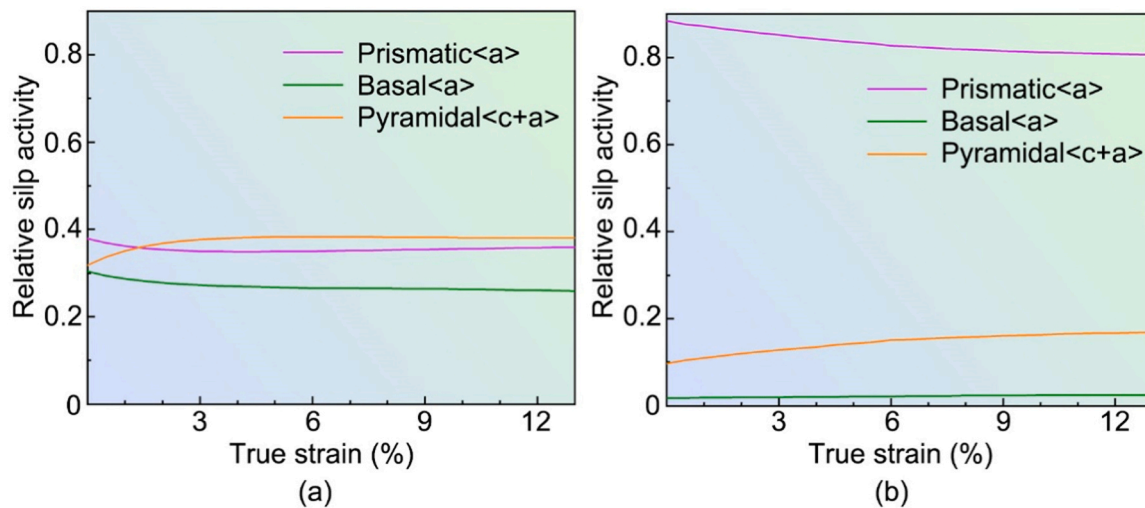
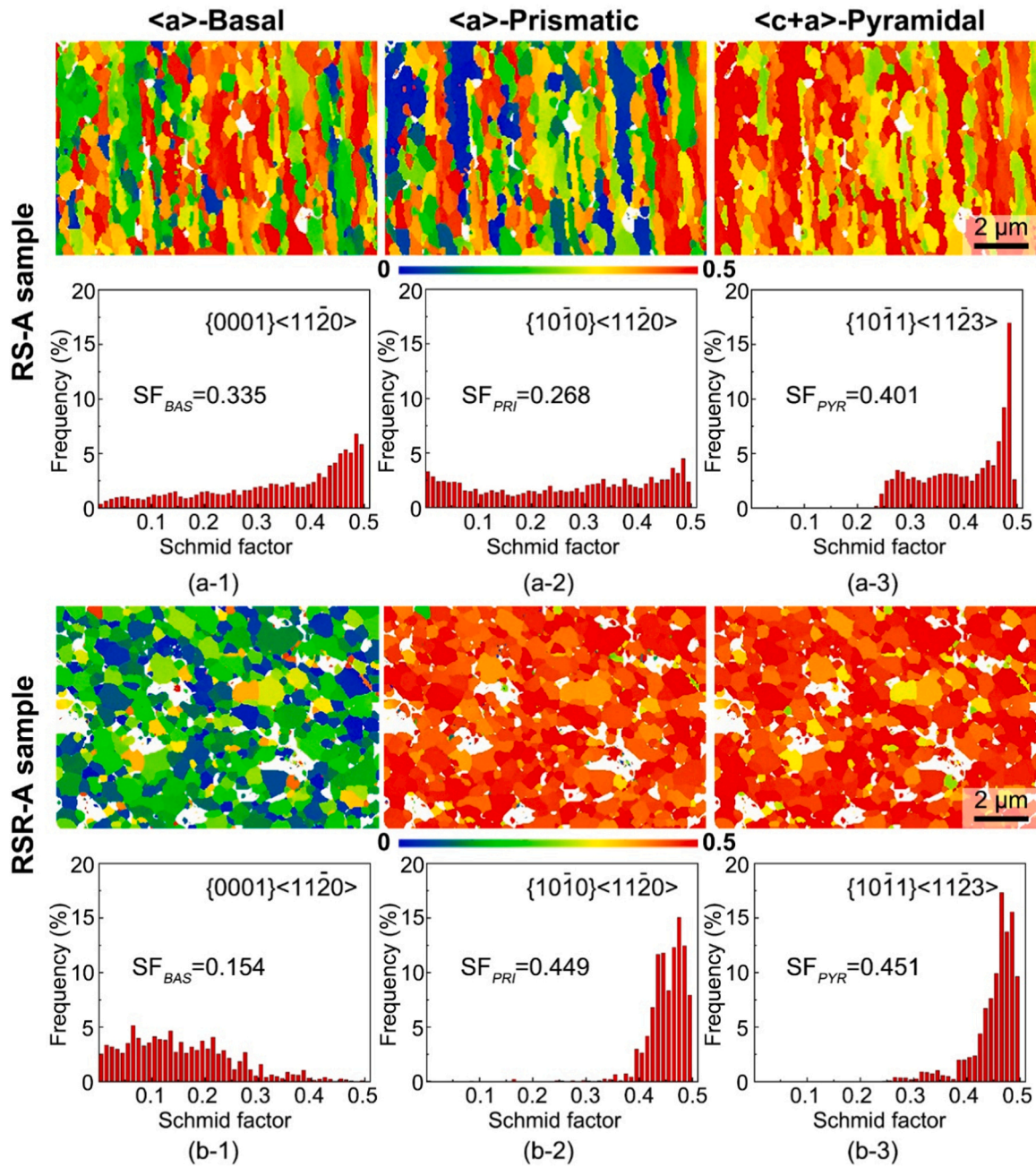


Fig. 9. Simulated relative activity plot for the three slip modes as a function of the true strain according to the visco-plastic self-consistent (VPSC) simulation: (a) rotary swaged sample after annealed (RS-A); (b) rotary swaging-rolled sample after annealed (RSR-A).



**Fig. 10.** Schmid factor distributions of different slip system: (a-1), (a-2) and (a-3) Basal  $\langle a \rangle$  slip, Prismatic  $\langle a \rangle$  slip and Pyramidal  $\langle c+a \rangle$  slip of rotary swaged sample after annealed (RS-A), respectively; (b-1), (b-2) and (b-3) Basal  $\langle a \rangle$  slip, Prismatic  $\langle a \rangle$  slip and Pyramidal  $\langle c+a \rangle$  slip of rotary swaging-rolled sample after annealed (RSR-A), respectively. The loading stress parallels to swaging direction (SD) or rolling direction (RD).

**Table 3**  
Applied stress (MPa) needed to generate different slip systems in rotary swaging (RS) and rotary swaging-rolling (RSR) samples after annealing.

Slip system	CRSS (MPa)	RS-A		RSR-A	
		m	Applied stress (MPa)	m	Applied stress (MPa)
Basal $\langle a \rangle$	150	0.335	447.7	0.154	974
Prismatic $\langle a \rangle$	30	0.268	112	0.449	66.8
Pyramidal $\langle c+a \rangle$	120	0.401	299	0.451	266.1

low mobility of  $\langle c+a \rangle$  dislocations and their tendency to pile up, enhancing the material's work hardening response. To sum up, the superior work hardening ability of the RS-A sample can be attributed to the

activation of more slip systems and the generation of  $\langle c+a \rangle$  dislocations, which significantly contribute to the strengthening of the material during deformation.

Despite the high work hardening ability observed in the RS-A sample, it does not translate to correspondingly high uniform elongation. This phenomenon can be explained through the lens of dislocation storage capacity. In the RS-A sample, the activation of multiple dislocation slip systems during deformation leads to a rapid increase in dislocation density. This corresponds to a higher work hardening ability in the early stage of deformation. However, the rapid increase in dislocation density also leads to a rapid decrease in dislocation storage capacity. Therefore, the space available for accommodating further dislocation proliferation decreases as deformation progresses, leading to a reduction in work hardening ability. In contrast, the RSR-A sample, which primarily

activates a single slip mode, exhibits low work hardening ability in the early stages of deformation. As strain continues to increase, dislocation density gradually accumulates, increasing the likelihood of dislocation interactions. This leads to an improvement in work hardening ability over time. The decrease in dislocation storage space in the RSR-A sample is more gradual, leading to a relatively steady work hardening ability and delaying the onset of necking. For HCP metals, although the activation of  $\langle c+a \rangle$  dislocations can coordinate deformation along the  $c$ -axis and improve work hardening ability, it also leads to a rapid accumulation of dislocation density in the early stages of deformation. The rapid accumulation consumes the material's potential for uniform deformation in the later stages. Thus, high work hardening ability early in the deformation process is not conducive to promoting uniform elongation of the material.

Achieving a balanced allocation of work hardening ability throughout different stages of plastic deformation can significantly enhance ductility. For example, Sun et al. engineered phase stability in a Ti alloy through metastable engineering to create a graded multi-stage activation of work hardening during tensile deformation [46]. Similarly, C.T. Liu et al. utilized additive manufacturing to achieve a gradient distribution of beta phase stabilizing elements in Ti alloys [47]. This design caused regions with poor stability to undergo stress-induced martensitic transformation (SIMT) first, followed by more stable regions, effectively regulating work hardening and enhancing ductility. In steel, the Lüders bands phenomenon serves as a typical example of how distributing work hardening can improve ductility [48]. During the early stage of deformation, the expansion of the Lüders bands results in a very low work hardening rate with minimal dislocation multiplication. Once this stage is completed, the material begins to exhibit traditional work hardening behavior. This delay in work hardening often significantly improves ductility, as has also been confirmed in recent studies on multi-principal element alloys [49]. In this study, for UFG pure Ti with an HCP structure, work hardening arises from the activation of dislocations (due to twinning is inhibited), therefore, the work hardening ability is closely related to the type and extent of dislocation activation, which can be regulated by adjusting the texture type. In the RS-A samples, due to the unique texture generated by RS, the three slip systems

can be activated simultaneously in early stage of tensile deformation, resulting in a high rate of dislocation multiplication and a significant improvement in work hardening ability. However, this process also rapidly reduces the dislocation storage capacity, leading to a rapid decrease in work hardening ability in the later stages of deformation, thereby decrease ductility. By adjusting the texture type through rolling, basal  $\langle a \rangle$  slip system is suppressed in the RSR-A sample, reduce the rate of dislocation multiplication in the early stage of tensile deformation. In addition, although the SF of prismatic  $\langle a \rangle$  and pyramidal  $\langle c+a \rangle$  slip systems are similar, the lower CRSS of the prismatic  $\langle a \rangle$  slip system leads to its dominated deformation behavior. While a small amount of activated  $\langle c+a \rangle$  dislocations can assist in uniform deformation. As the deformation increases,  $\langle c+a \rangle$  dislocations are gradually activated, resulting in a smooth work hardening behavior, achieves higher ductility. Overall, for UFG pure Ti with dislocation slip as the main deformation mode, adjusting its texture type through different deformation processes is an effective way to regulate its work hardening behavior. This strategy of adjusting work hardening behavior to achieve high ductility can be illustrated in Fig. 11.

In sum, the key to achieving higher uniform elongation lies in a judicious allocation of work hardening ability throughout the entire stretching process, instead of merely pursuing high work hardening ability. This strategy ensures that the material can accommodate more uniform deformation, thereby delaying necking and enhancing overall ductility.

## 5. Summary

In this study, severe plastic deformation of pure Ti was carried out by rotary swaging and rotary swaging combined with rolling. After annealing, the ultra-fine grained pure Ti samples were obtained characterized by fiber grains or equiaxed grains. Despite having similar grain sizes, they exhibited different textures, resulting in comparable yield strengths but significantly different work hardening behavior during tensile testing. Specifically, high uniform elongation and ductility were associated with low work hardening, while high work hardening corresponded to low ductility. In order to reveal this anomalous

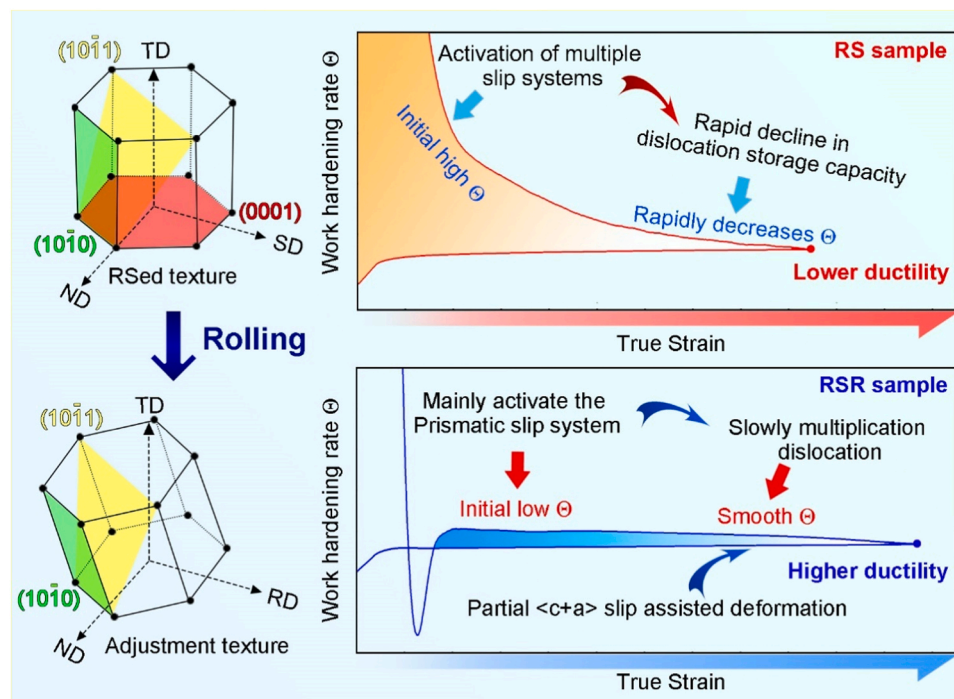


**Fig. 11.** Schematic representation of adjusting work hardening rate  $\Theta$  to achieve high ductility. The implementation of this strategy is based on adjusting the texture type of metal materials through plastic deformation.

phenomenon, the deformation behaviors of the rotary swaged sample after annealed (RS-A) and rotary swaging-rolled sample after annealed (RSR-A) were systematically investigated by TEM and visco-plastic self-consistent (VPSC) simulation. The key findings of this work are summarized as follows:

- (1) The work hardening exponent ( $n$ ) of RS-A and RSR-A samples during deformation was simulated using the Ludwick equation. The  $n$  value of RS-A sample was consistently higher than that of the RSR-A sample. However, segmented fitting results showed a decrease in the  $n$  value for RS-A samples with increasing strain, while RSR-A samples exhibited an increasing trend, surpassing RS-A samples in the later stages of deformation.
- (2) The active slip systems in RS-A and RSR-A samples during deformation were identified by two-beam bright-field TEM technology. The results shows that the RS-A sample activated both  $\langle a \rangle$  and  $\langle c+a \rangle$  type dislocations during deformation, while RSR-A samples predominantly activated  $\langle a \rangle$  dislocations.
- (3) VPSC simulation was employed to examine dislocation activities in ultrafine-grained pure Ti at the mesoscopic scale. The simulation supported that RS-A samples could activate basal, prismatic and pyramidal plane sliding modes, while RSR-A samples struggled to activate basal plane sliding mode. This difference was strongly correlated with the texture type of the samples. Overall the superior work hardening ability of the RS-A sample was resulted from the activation of more slip systems and the generation of  $\langle c+a \rangle$  dislocations.
- (4) The activation of multiple slip systems in the early stage of deformation endowed the RS-A sample with a higher ability for dislocation proliferation and work hardening. However, this rapid accumulation of dislocation density led to a decrease in dislocation storage space, causing a rapid decrease in work hardening ability. Therefore, the RSR-A sample, with its more limited slip system activation, exhibited a lower initial work hardening ability. As strain increased, the gradual accumulation of dislocations improved its work hardening ability, resulting in a more stable dislocation storage capacity and delayed necking, thereby enhancing uniform elongation.

#### CRedit authorship contribution statement

**Hao Zhou:** Writing – review & editing, Resources. **Yonghao Zhao:** Writing – review & editing, Supervision, Conceptualization. **Jiajun Hu:** Writing – original draft, Methodology, Investigation. **Dongmei Zhang:** Methodology, Investigation. **Zhaohua Hu:** Project administration, Funding acquisition. **Shuaizhuo Wang:** Validation, Data curation. **Lirong Xiao:** Validation, Investigation. **Bo Gao:** Visualization, Project administration. **Dongdi Yin:** Supervision, Resources.

#### Declaration of Competing Interest

The authors declare that they have no known competing financial interests or personal relationships that could have appeared to influence the work reported in this paper.

#### Acknowledgments

This work was supported by the National Key R&D Program of China (grant number 2021YFA1200203), the Key Program of National Natural Science Foundation of China (grant number 51931003), Jiangsu Province Leading Edge Technology Basic Research Major Project (BK20222014), the National Natural Science Foundation of China (grant numbers 51971112, 52171118, 52071178, 52201124), the Project Internationalized Construction of Teachers of Jiangsu University (grant number 4023000059), the Fundamental Research Funds for the Central Universities (Grant No. 30919011405).

The authors also want to acknowledge the support of the Jiangsu Key Laboratory of Advanced Micro-Nano Materials and Technology. SEM, TEM and EBSD experiments are performed at the Materials Characterization and Research Center of Nanjing University of Science and Technology.

#### References

- [1] Wang, X., Morisada, Y., Ushioda, K., Fujii, H., 2022. Double-sided friction stir spot welding of ultra-high strength C-Mn-Si martensitic steel by adjustable probes. *J. Mater. Process. Technol.* 300, 117422 <https://doi.org/10.1016/j.jmatprot.2021.117422>.
- [2] Trujillo-Tadeo, J.J., Arruebarrena, G., Dorantes-Rosales, H.J., Bilbao, Y., Vicario, I., Guraya, T., Hurtado, I., 2023. Design and characterization of a novel lightweight multicomponent alloy Al58Zn28Mg6Si8. *J. Mater. Res. Technol.* 27, 3751–3760. <https://doi.org/10.1016/j.jmrt.2023.10.102>.
- [3] Essa, A., Abeyathna, B., Rolfe, B., Weiss, M., 2023. Incremental shape rolling of top-hat shaped automotive structural and crash components. *J. Mater. Process. Technol.* 321, 118162 <https://doi.org/10.1016/j.jmatprot.2023.118162>.
- [4] Shen, F., Wang, H., Liu, Z., Liu, W., Könemann, M., Yuan, G., Wang, G., Münstermann, S., Lian, J., 2022. Local formability of medium-Mn steel. *J. Mater. Process. Technol.* 299, 117368 <https://doi.org/10.1016/j.jmatprot.2021.117368>.
- [5] Zheng, K., He, Z., Qu, H., Chen, F., Han, Y., Zheng, J.-H., Li, N., 2023. A novel quench-form and in-die creep age process for hot forming of 2219 thin aluminum sheets with high precision and efficiency. *J. Mater. Process. Technol.* 315, 117931 <https://doi.org/10.1016/j.jmatprot.2023.117931>.
- [6] Dong, H., Li, X., Li, Y., Zhao, S., Wang, H., Liu, X., Meng, B., Du, K., 2023. The anomalous negative electric current sensitivity of a precipitation hardened Al alloy during electrically-assisted forming. *J. Mater. Res. Technol.* 24, 9356–9368. <https://doi.org/10.1016/j.jmrt.2023.05.161>.
- [7] Ma, Z., Ye, J., Ma, Q., He, H., Chen, F., Zhang, Y., Wang, C., 2023. Deformation behavior of pure titanium foils in ultrasonic-assisted tensile forming process. *J. Mater. Process. Technol.* 319, 118093 <https://doi.org/10.1016/j.jmatprot.2023.118093>.
- [8] Jia, D., Wang, Y.M., Ramesh, K.T., Ma, E., Zhu, Y.T., Valiev, R.Z., 2001. Deformation behavior and plastic instabilities of ultrafine-grained titanium. *Appl. Phys. Lett.* 79, 611–613. <https://doi.org/10.1063/1.1384000>.
- [9] Ovid'ko, I.A., Valiev, R.Z., Zhu, Y.T., 2018. Review on superior strength and enhanced ductility of metallic nanomaterials. *Prog. Mater. Sci.* 94, 462–540. <https://doi.org/10.1016/j.pmatsci.2018.02.002>.
- [10] Zhao, S., Zhang, R., Yu, Q., Ell, J., Ritchie, R.O., Minor, A.M., 2021. Cryoforged nanotwinned titanium with ultrahigh strength and ductility. *Science* 373, 1363–1368. <https://doi.org/10.1126/science.abe7252>.
- [11] Weertman, J.R., Farkas, D., Hemker, K., Kung, H., Mayo, M., Mitra, R., Swygenhoven, H.V., 1999. Structure and Mechanical Behavior of Bulk Nanocrystalline Materials. *MRS Bull.* 24, 44–53. <https://doi.org/10.1557/S088376940005154X>.
- [12] Hu, J., Li, X., Zhang, Z., Wang, L., Li, Y., Xu, W., 2023. Overcoming the strength-ductility trade-off in metastable dual-phase heterogeneous structures using variable temperature rolling and annealing. *Mater. Res. Lett.* 11, 648–654. <https://doi.org/10.1080/21663831.2023.2209596>.
- [13] Xu, X.N., Li, H.J., Sun, B.Z., Tian, Y., Ye, Q.B., 2023. Enhanced strength-ductility-toughness synergy in an HSLA steel with multi-gradient ultrafine grained structure by adopting a two-stage rolling coupling inter-pass ultra-fast cooling process. *J. Mater. Process. Technol.* 313, 117832 <https://doi.org/10.1016/j.jmatprot.2022.117832>.
- [14] Qiao, Y., Wang, X., Liu, Z., Wang, E., 2013. Effects of grain size, texture and twinning on mechanical properties and work-hardening behaviors of pure Mg. *Mater. Sci. Eng.: A* 578, 240–246. <https://doi.org/10.1016/j.msea.2013.04.094>.
- [15] Cheng, X., Cai, P., Zhang, L., Chai, L., 2023. Unusual work hardening rate of a 3D gradient high purity Ti fabricated by laser surface treatment. *Mater. Sci. Eng.: A* 862, 144417. <https://doi.org/10.1016/j.msea.2022.144417>.
- [16] Zhu, Y., Wu, X., 2023. Heterostructured materials. *Prog. Mater. Sci.* 131, 101019 <https://doi.org/10.1016/j.pmatsci.2022.101019>.
- [17] Gong, J., Wilkinson, A.J., 2009. Anisotropy in the plastic flow properties of single-crystal  $\alpha$  titanium determined from micro-cantilever beams. *Acta Mater.* 57, 5693–5705. <https://doi.org/10.1016/j.actamat.2009.07.064>.
- [18] Chen, W., Xu, J., Liu, D., Bao, J., Sabbaghianrad, S., Shan, D., Guo, B., Langdon, T. G., 2020. Microstructural Evolution and Microhardness Variations in Pure Titanium Processed by High-Pressure Torsion. *Adv. Eng. Mater.* 22, 1901462. <https://doi.org/10.1002/adem.201901462>.
- [19] Wang, C.T., Fox, A.G., Langdon, T.G., 2014. Microstructural evolution in ultrafine-grained titanium processed by high-pressure torsion under different pressures. *J. Mater. Sci.* 49, 6558–6564. <https://doi.org/10.1007/s10853-014-8248-6>.
- [20] Zhao, X., Yang, X., Liu, X., Wang, X., Langdon, T.G., 2010. The processing of pure titanium through multiple passes of ECAP at room temperature. *Mater. Sci. Eng.: A* 527, 6335–6339. <https://doi.org/10.1016/j.msea.2010.06.049>.
- [21] Mertová, K., Salveter, P., Duchek, M., 2020. Comparison of cryogenic and cold deformation of commercially pure titanium. *Mater. Today.: Proc.* 28, 916–919. <https://doi.org/10.1016/j.matpr.2019.12.324>.
- [22] Mao, Q., Zhang, Y., Liu, J., Zhao, Y., 2021. Breaking Material Property Trade-offs via Macrodesign of Microstructure. *Nano Lett.* 21, 3191–3197. <https://doi.org/10.1021/acs.nanolett.1c00451>.

- [23] Cao, Y., Ni, S., Liao, X., Song, M., Zhu, Y., 2018. Structural evolutions of metallic materials processed by severe plastic deformation. *Mater. Sci. Eng.: R: Rep.* 133, 1–59. <https://doi.org/10.1016/j.mser.2018.06.001>.
- [24] Yu, Q., Shan, Z.-W., Li, J., Huang, X., Xiao, L., Sun, J., Ma, E., 2010. Strong crystal size effect on deformation twinning. *Nature* 463, 335–338. <https://doi.org/10.1038/nature08692>.
- [25] Huang, Z., Wen, D., Jiang, X., Wang, A., Li, Y., Cao, Y., Hou, X., Wang, B., Zhu, Y., 2022. Additional dislocation slip determined excess yield stress in titanium. *Mater. Sci. Eng.: A* 861, 144387. <https://doi.org/10.1016/j.msea.2022.144387>.
- [26] Yu, Q., Sun, J., Morris, J.W., Minor, A.M., 2013. Source mechanism of non-basal (c + a) slip in Ti alloy. *Scr. Mater.* 69, 57–60. <https://doi.org/10.1016/j.scriptamat.2013.03.009>.
- [27] Gu, L., Meng, A., Chen, X., Zhao, Y., 2023. Simultaneously enhancing strength and ductility of HCP titanium via multi-modal grain induced extra dislocation hardening. *Acta Mater.* 252, 118949 <https://doi.org/10.1016/j.actamat.2023.118949>.
- [28] Tesář, K., Koller, M., Vokoun, D., Tyc, O., Čech, J., Sedlák, P., 2023. Texture, elastic anisotropy and thermal stability of commercially pure titanium prepared by room temperature ECAP. *Mater. Des.* 226, 111678 <https://doi.org/10.1016/j.matdes.2023.111678>.
- [29] Wang, T., Zha, M., Du, C., Jia, H.-L., Wang, C., Guan, K., Gao, Y., Wang, H.-Y., 2023. High strength and high ductility achieved in a heterogeneous lamella-structured magnesium alloy. *Mater. Res. Lett.* 11, 187–195. <https://doi.org/10.1080/21663831.2022.2133976>.
- [30] Meng, A., Chen, X., Nie, J., Gu, L., Mao, Q., Zhao, Y., 2021. Microstructure evolution and mechanical properties of commercial pure titanium subjected to rotary swaging. *J. Alloy. Compd.* 859, 158222 <https://doi.org/10.1016/j.jallcom.2020.158222>.
- [31] Liu, N., Wang, Y., He, W., Li, J., Chapuis, A., Luan, B., Liu, Q., 2018. Microstructure and textural evolution during cold rolling and annealing of commercially pure titanium sheet. *Trans. Nonferrous Met. Soc. China* 28, 1123–1131. [https://doi.org/10.1016/S1003-6326\(18\)64748-X](https://doi.org/10.1016/S1003-6326(18)64748-X).
- [32] Li, X., Sun, B.-H., Guan, B., Jia, Y.-F., Gong, C.-Y., Zhang, X.-C., Tu, S.-T., 2021. Elucidating the effect of gradient structure on strengthening mechanisms and fatigue behavior of pure titanium. *Int. J. Fatigue* 146, 106142. <https://doi.org/10.1016/j.ijfatigue.2021.106142>.
- [33] Ludwick, P., 1909. *Element der technologischen mechanik*. Springer verlag,, Berlin.
- [34] Zhang, D., Zhang, M., Lin, R., Liu, G., Li, J., Feng, Y., 2021. Strengthening and strain hardening mechanisms of a plain medium carbon steel by multiscale lamellar structures. *Mater. Sci. Eng.: A* 827, 142091. <https://doi.org/10.1016/j.msea.2021.142091>.
- [35] Chen, J., Han, Y., Wei, Z., Li, S., Sun, Z., Zhang, L., Huang, G., Le, J., Zhang, D., Lu, W., 2023. Heterostructured titanium composites with superior strength-ductility synergy via controllable bimodal grains and dislocation activity. *Mater. Res. Lett.* 11, 863–871. <https://doi.org/10.1080/21663831.2023.2252858>.
- [36] Sahu, V.K., Yadava, M., Chakraborty, P., Gurao, N.P., 2022. Effect of notch severity and crystallographic texture on local deformation and damage in commercially pure titanium. *Int. J. Plast.* 155, 103318 <https://doi.org/10.1016/j.ijplas.2022.103318>.
- [37] Lebensohn, R.A., Tomé, C.N., 1993. A self-consistent anisotropic approach for the simulation of plastic deformation and texture development of polycrystals: application to zirconium alloys. *Acta Metall. Et. Mater.* 41, 2611–2624. [https://doi.org/10.1016/0956-7151\(93\)90130-K](https://doi.org/10.1016/0956-7151(93)90130-K).
- [38] Hu, L., Lv, H., Shi, L., Chen, Y., Chen, Q., Zhou, T., Li, M., Yang, M., 2022. Research on deformation mechanism of AZ31 magnesium alloy sheet with non-basal texture during uniaxial tension at room temperature: a visco-plastic self-consistent analysis. *J. Magnes. Alloy.* 10, 1994–2008. <https://doi.org/10.1016/j.jma.2020.12.008>.
- [39] Bozzolo, N., Dewobroto, N., Wenk, H.R., Wagner, F., 2007. Microstructure and microtexture of highly cold-rolled commercially pure titanium. *J. Mater. Sci.* 42, 2405–2416. <https://doi.org/10.1007/s10853-006-1302-2>.
- [40] Zhou, B., Wang, L., Wang, J., Maldar, A., Zhu, G., Jia, H., Jin, P., Zeng, X., Li, Y., 2022. Dislocation behavior in a polycrystalline Mg-Y alloy using multi-scale characterization and VPSC simulation. *J. Mater. Sci. Technol.* 98, 87–98. <https://doi.org/10.1016/j.jmst.2021.03.087>.
- [41] Chen, W., Wu, W., Wang, W., Zhang, W., Liu, X., Kim, H.S., 2023. Adjusting approaches of basal texture for improvement of tension-compression asymmetry in extruded magnesium alloys. *Mater. Res. Lett.* 11, 563–570. <https://doi.org/10.1080/21663831.2023.2189635>.
- [42] Huang, Z.W., Yong, P.L., Zhou, H., Li, Y.S., 2020. Grain size effect on deformation mechanisms and mechanical properties of titanium. *Mater. Sci. Eng.: A* 773, 138721. <https://doi.org/10.1016/j.msea.2019.138721>.
- [43] Lütjering, G., Williams, J.C., 2007. *Titanium*. Springer,, Berlin Heidelberg.
- [44] Wu, X., Kalidindi, S., Necker, C., Salem, A., 2007. Prediction of crystallographic texture evolution and anisotropic stress-strain curves during large plastic strains in high purity  $\alpha$ -titanium using a Taylor-type crystal plasticity model. *Acta Mater.* 55, 423–432. <https://doi.org/10.1016/j.actamat.2006.08.034>.
- [45] Deka, N., Alleman, C., Medlin, D.L., Sills, R.B., 2023. Energy and stochasticity: the yin and yang of dislocation patterning. *Mater. Res. Lett.* 11, 289–295. <https://doi.org/10.1080/21663831.2022.2149283>.
- [46] Zhang, C., Liu, S., Zhang, J., Zhang, D., Kuang, J., Bao, X., Liu, G., Sun, J., 2023. Trifunctional nanoprecipitates ductilize and toughen a strong laminated metastable titanium alloy. *Nat. Commun.* 14, 1397. <https://doi.org/10.1038/s41467-023-37155-y>.
- [47] Zhang, T., Huang, Z., Yang, T., Kong, H., Luan, J., Wang, A., Wang, D., Kuo, W., Wang, Y., Liu, C.-T., 2021. In situ design of advanced titanium alloy with concentration modulations by additive manufacturing. *Science* 374, 478–482. <https://doi.org/10.1126/science.abj3770>.
- [48] He, B.B., Hu, B., Yen, H.W., Cheng, G.J., Wang, Z.K., Luo, H.W., Huang, M.X., 2017. High dislocation density-induced large ductility in deformed and partitioned steels. *Science* 357, 1029–1032. <https://doi.org/10.1126/science.aan0177>.
- [49] Xu, B., Duan, H., Chen, X., Wang, J., Ma, Y., Jiang, P., Yuan, F., Wang, Y., Ren, Y., Du, K., Wei, Y., Wu, X., 2024. Harnessing instability for work hardening in multi-principal element alloys. *Nat. Mater.* <https://doi.org/10.1038/s41563-024-01871-7>.